Petroleum Science 23 (2026) 5418–5432

Contents lists available at ScienceDirect

Petroleum Science

journal homepage: www.keaipublishing.com/en/journals/petroleum-science

Original Paper

Trans-layer inversion of logging-while-drilling azimuthal electromagnetic measurements guided by multi-boundary detection capability assessment

Yan-Xue Wang [a,b,c], Lei Wang [a,b,c,*], Xin-Min Ge [a,b,c], Yi-Ren Fan [a,b,c]

[a] School of Geosciences, China University of Petroleum (East China), Qingdao, 266580, Shandong, China
[b] State Key Laboratory of Deep Oil and Gas, China University of Petroleum (East China), Qingdao, 266580, Shandong, China
[c] CNPC Key Laboratory for Well Logging, China University of Petroleum (East China), Qingdao, 266580, Shandong, China

ARTICLE INFO

Article history:
Received 18 December 2025
Received in revised form
21 February 2026
Accepted 27 April 2026
Available online 30 April 2026

Edited by Meng-Jiao Zhou

Keywords:
Logging-while-drilling azimuthal electromagnetic measurements
Multi-boundary detection
Adaptive modeling strategy
Trans-layer inversion
Geosteering

ABSTRACT

The inversion of logging-while-drilling azimuthal electromagnetic measurements is essential for geosteering in horizontal wells and optimizing reservoir development. Conventional fixed-layer inversion models lack adaptability to dynamically varying formations, resulting in limited applicability and a trade-off between accuracy and efficiency. This study introduces a trans-layer inversion method that adaptively optimizes model complexity. The method quantifies the tool's multi-boundary detection capability using eigenvalue analysis of the Fisher information matrix. Statistical analysis of synthetic models informs the construction of an inversion model library spanning two-to five-layer configurations, facilitating adaptation to diverse formation geometries. To address the dependence of multi-layer inversion on initial values, a progressively increasing model complexity hot-start mechanism is implemented, allowing lower-order inversion results to constrain higher-order models. A comprehensive quality score autonomously selects the optimal inversion model. Numerical examples demonstrate that: (1) in a three-layer sand-shale sequence, the method enhances early recognition of reservoir boundaries due to the model library's coverage of all tool positions; (2) in a six-layer thin-bed model, the trans-layer inversion reduces mean square error by 91.5% compared to conventional three-layer inversion, significantly improves thin-bed imaging resolution, and doubles computational efficiency relative to fixed five-layer inversion; (3) in an anticlinal reservoir model, the method accurately tracks both reservoir structure and internal oil-water contacts; (4) field data validation from a complex clastic reservoir confirms the method's ability to delineate thin shale layers and guide well trajectory in real drilling scenarios. This approach offers a robust solution to the challenges of model applicability and computational efficiency in LWD inversion.

1. Introduction

Geosteering in horizontal wells is a critical technology for reducing drilling risks and optimizing hydrocarbon production by enabling real-time identification of formation boundaries and oil/water contact (OWC) (Tian et al., 2023; Jia et al., 2024; Wang et al., 2025; Hong et al., 2022). Logging-while-drilling (LWD) azimuthal electromagnetic tools (AETs) have become the cornerstone of geosteering and well placement (Bittar et al., 2009; Wang et al., 2007; Beer et al., 2010; Liu et al., 2025). Leveraging their depth of investigation and high azimuthal resolution, AETs significantly improve reservoir exposure rates and provide essential data for real-time geological model updates (Omeragic et al., 2006; Nardi et al., 2010; Wang et al., 2021; Yang et al., 2025). The continuous development of commercial AETs has progressively extended the boundary detection range from approximately 4.5 m to over 7.5 m, enhancing their ability to sense remote formations (Yang et al., 2020; Sun et al., 2021; Wu et al., 2018, 2022a; Yue et al., 2022). However, this expanded depth of investigation also increases the

* Corresponding author.
E-mail address: leiwang1989@upc.edu.cn (L. Wang).
Peer review under the responsibility of China University of Petroleum (Beijing).

https://doi.org/10.1016/j.petsci.2026.04.044
1995-8226/

influence of surrounding layered formations, resulting in more complex log responses and substantially elevating the challenges for inversion interpretation.

The inversion of azimuthal electromagnetic measurements confronts two interrelated challenges: model parameterization and iterative optimization. Accurate model construction requires the parameterization to faithfully represent the actual stratigraphic geometry encountered during drilling (Wu et al., 2022b). While increased model complexity enhances representational capability, it simultaneously introduces more parameters, aggravating solution non-uniqueness. The optimization process needs to balance global search capability and computational efficiency. Given the stringent constraints of real-time data processing, one-dimensional parametric inversion methods are widely adopted in the industry (Zhou et al., 2016; Hu et al., 2018; Yu et al., 2024; Shen et al., 2018). These approaches generally fall into two categories: deterministic single-/dual-boundary inversion and multi-boundary stochastic inversion.

Deterministic inversion employs efficient local optimization algorithms such as Gauss-Newton or Levenberg-Marquardt, often supplemented with multiple initialization strategies to mitigate convergence to local minima. The method's computational efficiency and minimal parameter requirements have established it as the mainstream technique for real-time geosteering in formations with layer thickness exceeding approximately 1 m (Wang et al., 2018; Wang & Fan, 2019; Pardo and Torres-Verdín, 2015; Li et al., 2023). As the industry increasingly targets complex reservoirs, research into multi-layer inversion has gained momentum. However, these problems involve substantially larger parameter spaces and exhibit strong non-uniqueness. Deterministic algorithms frequently struggle to converge reliably without high-quality initial models, while global stochastic intelligent optimization methods—such as particle swarm optimization and Markov Chain Monte Carlo (MCMC)—though reducing dependency on initial guesses through extensive sampling, incur computational costs that remain prohibitive for real-time applications (Yan et al., 2018; Shen et al., 2018; Kang et al., 2023; Ciabarri et al., 2023; Sviridov et al., 2023).

The fundamental limitation of existing inversion frameworks lies in their fixed model complexity. Oversimplified models, while computationally efficient, often fail to capture meticulous geological features, leading to interpretation errors (Nardi et al., 2010). Conversely, overly complex models suffer from expanded parameter spaces that exacerbate non-uniqueness and impede convergence (Dupuis and Denichou, 2015; Wang et al., 2019). This limitation becomes particularly pronounced when employing global stochastic optimization algorithms, whose computational demands far exceed practical limits for real-time processing. An elegant solution would dynamically select the simplest model that adequately explains the measured data, thereby avoiding parameter redundancy while maintaining geological fidelity. However, developing such an adaptive framework has been hindered by the absence of both quantitative methods for assessing a tool's sensitivity to multiple boundaries and principled approaches for selecting appropriate model dimensionality.

In this paper, a trans-layer inversion method is developed to address these challenges. Firstly, the Fisher information matrix is introduced to quantitatively assess the multi-boundary detection capability of AETs. Analysis of typical sedimentary environments indicates that two to four boundaries can be detected. Based on this assessment, an inversion model library is established. By incorporating a gradient-based algorithm with a multi-layer model initialization strategy, an adaptive trans-layer inversion workflow is constructed. A novel quality score mechanism enables autonomous selection of optimal model complexity during inversion. Numerical examples demonstrate that the proposed method strikes a better balance between accuracy and computational efficiency compared to conventional fixed three-layer and five-layer inversions.

2. Assessment of multi-boundary detection capability for azimuthal electromagnetic measurements

The detection capability of AETs forms the foundation for their application in geosteering and formation evaluation. This section aims to establish a quantitative assessment framework for detection capability, progressing from simple single-boundary models to complex multi-boundary formations. It starts with a single-boundary model assessment, extends to a multi-boundary model using the Fisher information matrix, and ends with statistical analysis to find practically detectable boundary numbers in common geological cases.

2.1. Detection capability assessment with a single-boundary model

The detection capability of AETs is fundamentally assessed based on the directional response to formation boundaries, known as the geosignal (Li et al., 2005). The geosignal is defined by the amplitude attenuation (Att) and phase shift (PS) between voltages measured by tilted receivers at different azimuths. Its key characteristic is a directionally sensitive, non-zero response that becomes significant only when the tool approaches a boundary. To quantify this capability within a tractable framework, the industry-standard approach adopts a single-boundary model (Li et al., 2005, 2020). In this model, the depth of detection (DOD) is defined as the distance-to-boundary at which the geosignal first equals a predefined detection threshold (Thr). As conceptually illustrated in Fig. 1, the DOD represents the furthest distance at which the boundary can be reliably identified from the geosignal decay profile. It is primarily governed by the tool configuration, including the transmitter-receiver spacing (L) and operating frequency (fre), the formation true resistivity (R_t), the shoulder bed resistivity (R_s), and the relative dip angle (α). This relationship can be expressed as:

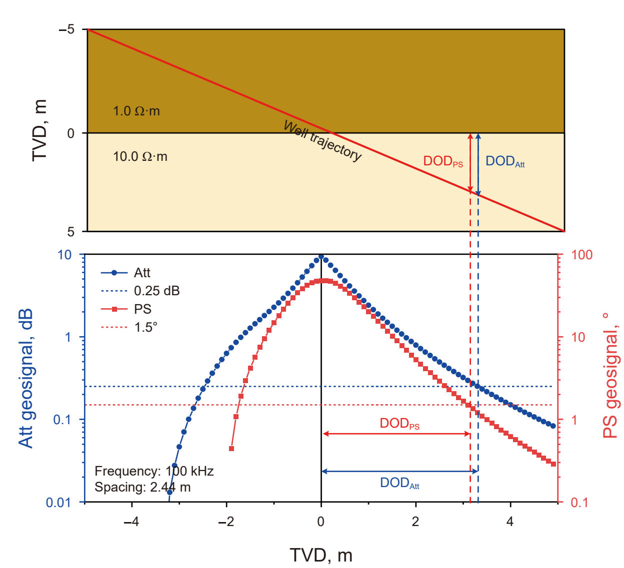

Fig. 1. Schematic definition of the DOD, DOD_{PS} and DOD_{Att} denote the detection depths derived from the phase shift (PS) and amplitude attenuation geosignals, respectively.

$$\mathrm{DOD} = f(R_t, R_s, L, \mathrm{fre}, \alpha, \mathrm{Thr}). \quad (1)$$

In the subsequent analysis, the tool is assumed to be parallel to the formation boundary ($\alpha = 90°$). By systematically varying the resistivities of the host layer and the adjacent layer, the boundary detection distance chart presented in Fig. 2 is generated. The tool is configured with a source spacing of 2.44 m and an operating frequency of 100 kHz, while the formation resistivity contrast ranges from 0.01 to 100. When the detection thresholds for the PS and Att are set to 1.5° and 0.25 dB, respectively, the resulting distribution of the maximum DOD is shown in Fig. 2(a). The detection range increases significantly when the tool is placed in a high-resistivity layer, reaching a maximum of 4.1 m. When the signal detection thresholds are reduced to 0.05° and 0.02 dB, the maximum DOD extends to 8.25 m. The corresponding distribution across formation and adjacent-layer resistivity contrasts is illustrated in Fig. 2(b).

This chart defines the theoretical upper limit of the tool's detection capability under ideal conditions. However, it overestimates practical performance because it does not account for the influence of noise in actual measurements. Noise in azimuthal electromagnetic measurements arises mainly from electronic noise, environmental interference, and source-coupled fluctuations. It can be modeled as a random voltage superimposed on the ideal received signal. When mapped to Att and PS signals, this corresponds to multiplicative relative errors and additive absolute errors, respectively. To quantitatively characterize the effect of noise, a Monte Carlo simulation is employed. After defining the single-boundary model parameters (R_t, R_s, α, and the distance to boundary d), tool configuration (L, fre), and detection thresholds (Thr), and assuming an ideal received voltage V_1^0, V_2^0, the standard deviation of the voltage noise at a given signal-to-noise ratio (SNR) is given by

$$\sigma_{V_j} = \left|V_j^0\right| \cdot 10^{-\frac{\mathrm{SNR}}{20}}, \quad j = 1, 2. \quad (2)$$

Two independent sets of N_{MC} complex Gaussian noise samples are then generated $N_j \sim \mathscr{CN}\left(0, \sigma_{V_j}\right)$, $j = 1, 2$, producing the noisy voltage:

$$V_1 = V_1^0 + N_1, \; V_2 = V_2^0 + N_2 \quad (3)$$

The i-th measured signal is expressed as

$$\begin{aligned} \triangle\phi_{\mathrm{meas}}^{(i)} &= \arg\left(V_2^{(i)}\right) - \arg\left(V_1^{(i)}\right) \\ \mathrm{Att}_{\mathrm{meas}}^{(i)} &= 20 \log_{10}\left(\frac{\left|V_2^{(i)}\right|}{\left|V_1^{(i)}\right|}\right) \end{aligned} , \quad (4)$$

where $V_1^{(i)}$ and $V_2^{(i)}$ denote the i-th measured noisy voltages. An indicator function I is defined as,

$$I^{(i)} = \begin{cases} 1, \text{if} \left|\triangle\phi_{\mathrm{meas}}^{(i)}\right| \geq \mathrm{Thr}_{\mathrm{PS}} \text{ or } \left|\mathrm{Att}_{\mathrm{meas}}^{(i)}\right| \geq \mathrm{Thr}_{\mathrm{Att}} \\ 0, \text{otherwise} \end{cases} \quad (5)$$

where $\mathrm{Thr}_{\mathrm{PS}}$ and $\mathrm{Thr}_{\mathrm{Att}}$ denote the phase shift and amplitude attenuation thresholds, respectively. The detection probability is calculated as the proportion of simulated measurements exceeding the threshold:

$$P(\mathrm{detect}|d) = \frac{1}{N_{\mathrm{MC}}} \sum_{i=1}^{N_{\mathrm{MC}}} I^{(i)}. \quad (6)$$

where N_{MC} denotes the number of Monte Carlo trials.

By varying the distance to the boundary, a curve of detection probability P versus distance is obtained. The effective detection distance d_{90} is defined as the distance at which $P = 90\%$. The uncertainty interval is defined as the distance range where P decreases from 90% to 10%, denoted as $\Delta d = |d_{90} - d_{10}|$. Fig. 3 illustrates the detection probability curves for Att and PS geosignals under resistivities of 10 and 1 Ω·m, with an SNR of 40 dB. The results are based on $N_{\mathrm{MC}} = 10000$ Monte Carlo trials, which ensure the estimated probability P is stable. The amplitude attenuation in this model achieves an effective detection distance of 2.99 m with an uncertainty interval of 0.28 m, while the PS yields an effective detection distance of 2.02 m with an uncertainty interval of 0.12 m.

To clearly quantify this influence of SNR, Table 1 summarizes the impact of SNR on both the effective detection distance (d_{90}) and the uncertainty range (Δd). For example, for the Att geosignal, the reliable detection distance contracts from 3.09 m to 2.65 m as the SNR decreases from 60 dB to 30 dB. This occurs because the geosignal from a distant boundary becomes weaker and falls

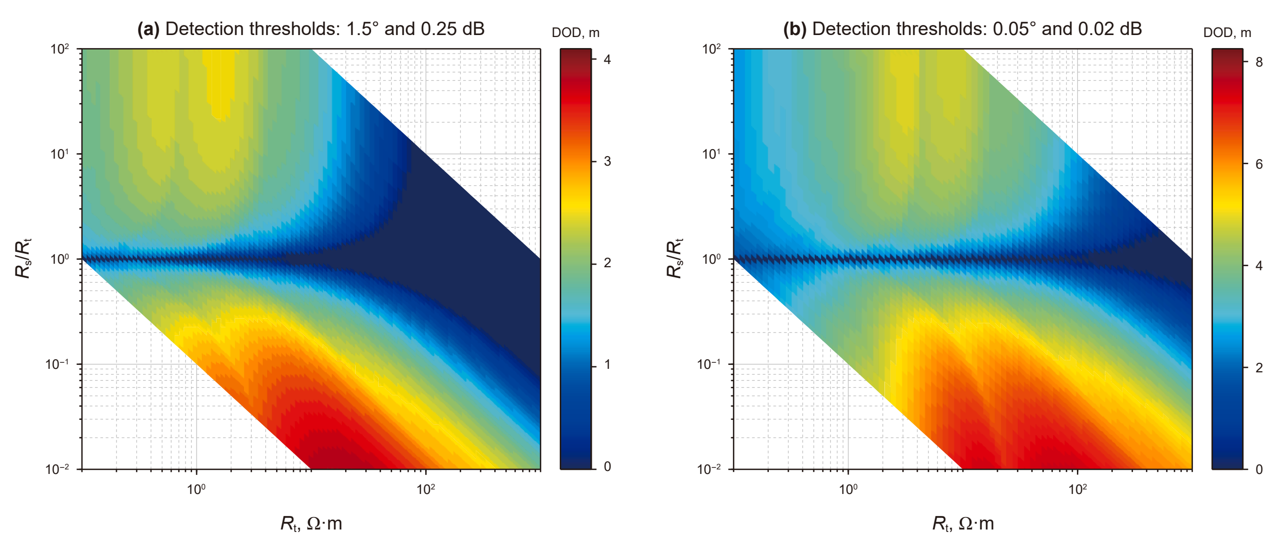

Fig. 2. Distribution of DOD to formation resistivity: **(a)** with detection thresholds set to 1.5° and 0.25 dB; **(b)** with detection thresholds set to 0.05° and 0.02 dB.

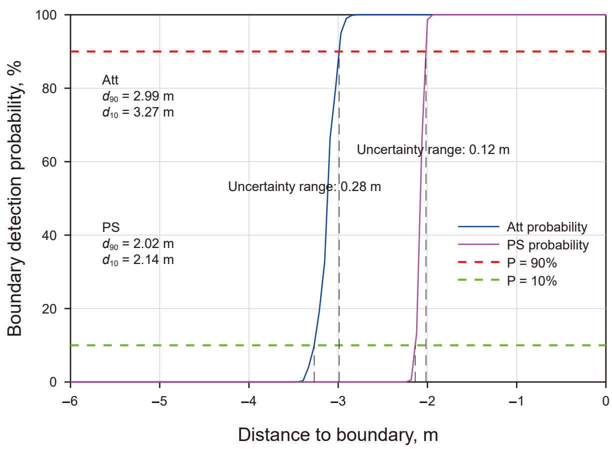

Fig. 3. Boundary detection probability curves for the single-boundary model.

Table 1
Impact of SNR on the detection performance of Att and PS geosignals.

SNR, dB	Att geosignal		PS geosignal	
	d_{90}, m	Δd, m	d_{90}, m	Δd, m
30	2.65	1.39	1.76	1.18
40	2.99	0.28	2.02	0.12
60	3.09	0.11	2.07	0.04

below a discernible level earlier when the noise floor is higher. More notably, the uncertainty range widens substantially with decreasing SNR: it is sharp and narrow ($\Delta d = 0.11$ m) at a high SNR of 60 dB, becomes broader ($\Delta d = 0.28$ m) at a moderate 40 dB, and exceeds 1 m at a low SNR of 30 dB, where the detection probability curve becomes so gradual that stable boundary identification becomes highly unreliable.

Taking the Att geosignal as an example, with a detection threshold set at 0.25 dB and an SNR of 40 dB, the resulting effective DOD map and associated uncertainty range are presented in Fig. 4. A more pronounced uncertainty range is observed in regions where the tool is located in higher-resistivity formations. The underlying physical mechanism can be explained as follows: high-resistivity formations attenuate electromagnetic waves less strongly, enhancing the tool's sensitivity to distant boundaries. However, the absolute variation in signals from these distant boundaries remains relatively small, making them susceptible to being obscured by noise and thus leading to an expanded uncertainty range.

The DOD assessment method, based on a single-boundary model, provides the foundation for characterizing tool detection performance. In horizontal drilling, however, the tool response couples multiple formations within its sensing volume, rendering conventional single-boundary DOD evaluation inadequate. A new theoretical framework is therefore required to quantitatively assess the tool's capability to resolve multi-layer formations.

2.2. Assessment of multi-boundary detection capability based on the Fisher information matrix

Assessing a tool's detection capability in multi-layer formations is fundamentally a parameter estimation problem. The central task is to evaluate the sensitivity of each formation parameter to the measured data. This sensitivity is quantified by the Jacobian matrix, which contains the partial derivatives of the forward model with respect to each parameter. To rigorously characterize parameter uncertainty, we employ the Fisher information matrix (FIM; e.g., Schervish, 1995; Pakrooh et al., 2015; Fischer, 2018), which encapsulates the information content of the data regarding all model parameters. The inverse of the FIM yields the Cramér–Rao lower bound (CRLB), defining the minimum achievable variance—and hence the best possible estimation accuracy—for any unbiased estimator under a given noise level.

Consider a layered model with n boundaries, parameterized by the vector $\mathbf{m} = [d_1, d_2, \ldots, d_i \ldots, d_n, R_0, R_1, \ldots, R_{i-1}, \ldots, R_n]^{\mathrm{T}}$, where d_i denotes the distance from the i-th boundary to the tool, and R_i represents the resistivity of the $(i+1)$-th layer. Under the assumption of additive Gaussian white noise, the measurement matrix $\mathbf{A}$ is normally distributed. The Fisher information matrix quantifies the information about the model parameters contained in the measured data and is defined as

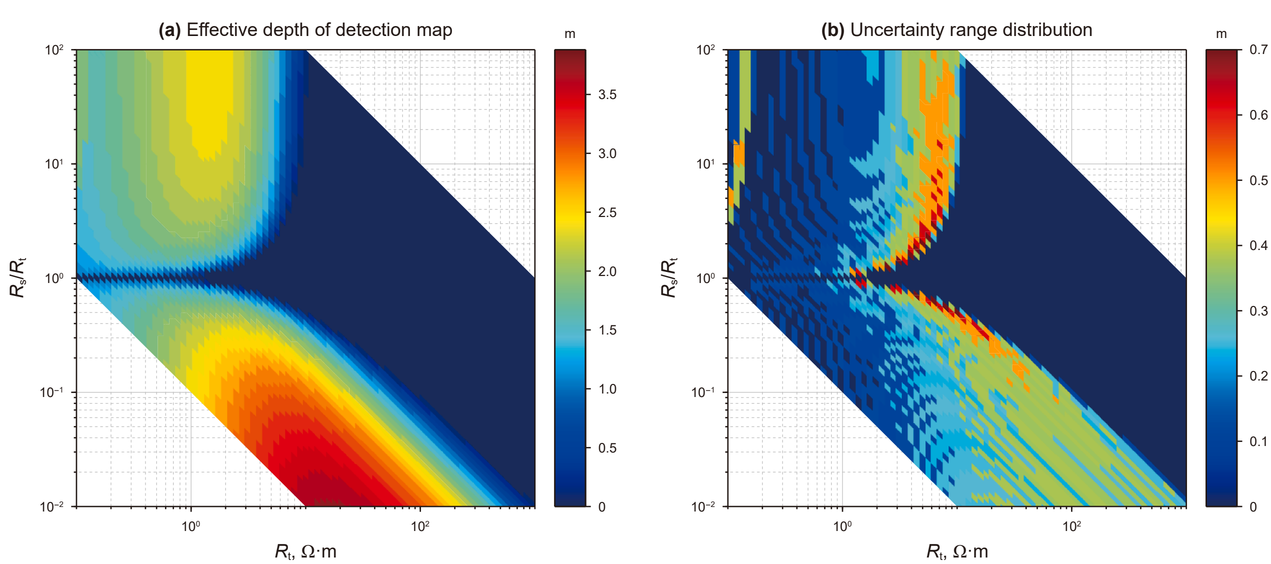

Fig. 4. Evaluation of detection capability for the Att geosignal: (**a**) effective DOD map; (**b**) uncertainty range distribution.

$$[\mathbf{F}(\mathbf{m})]_{j_1 j_2} = -\mathbf{E}\left[\frac{\partial^2}{\partial m_{j_1}\partial m_{j_2}}\log p(\mathbf{A}|\mathbf{m})\right] = \frac{1}{\sigma^2}\sum_{k=1}^{N_{\rm data}}\left(\frac{\partial f_k(\mathbf{m})}{\partial m_{j_1}}\right)\left(\frac{\partial f_k(\mathbf{m})}{\partial m_{j_2}}\right) = \frac{1}{\sigma^2}\mathbf{J}^{\rm T}(\mathbf{m})\cdot\mathbf{J}(\mathbf{m}), \tag{7}$$

where $\log p(\mathbf{A}|\mathbf{m})$ the log-likelihood function, $\mathbf{J}$ is the Jacobian matrix, $\mathbf{E}[\cdot]$ is the expectation operator, m_{j_1} is the j_1-th element of vector $\mathbf{m}$, and $N_{\rm data}$ denotes the number of the measurements. According to the Cramér–Rao theorem, the covariance matrix $\mathrm{Cov}(\mathbf{m})$ of any unbiased estimator satisfies:

$$\mathrm{Cov}(\mathbf{m}) \geq \mathbf{F}^{-1}(\mathbf{m}), \tag{8}$$

where $\mathbf{C} = \mathbf{F}^{-1}(\mathbf{m})$ is the Cramér–Rao lower bound matrix. The diagonal elements C_{jj} provide the minimum achievable variance for the i-th parameter. Thus, the standard deviation of the estimate for m_j satisfies:

$$\sigma_{m_j} \geq \sqrt{C_{jj}}. \tag{9}$$

The boundary d_i is considered theoretically resolvable if its lower-bound standard deviation σ_{d_i} does not exceed a specified tolerance $|\varepsilon|$. The number of boundaries satisfying this criterion defines the maximum number of reliably detectable boundaries under the given noise level. Additionally, the uncertainty range for each resolvable boundary position can be expressed as $[d_i - 2\sigma_{d_i},\ d_i + 2\sigma_{d_i}]$, corresponding to a 95% confidence interval.

The physical significance of using the inverse of the FIM to determine the best achievable estimation accuracy lies in its direct correspondence to a fundamental reality in well logging: when certain formation parameters exhibit low sensitivity to the measured data, the FIM becomes ill-conditioned (nearly singular). Consequently, the diagonal elements of its inverse grow very large, indicating that no inversion method can reliably determine those parameters—any estimate will be accompanied by substantial uncertainty.

To quantitatively assess how far a tool can "see" in multi-layer formations, we adopt the threshold detection concept introduced in Section 2.1. Consider a known multi-layer formation model with a fixed tool position as shown in Fig. 5, where the farthest reliably detectable boundary above the tool is denoted as d_i. Keeping all other formation parameters unchanged, we introduce a virtual boundary $d_{i'}$, beyond the existing boundary d_i. The resistivity of the layer between d_i and $d_{i'}$ is set to R_i, while the resistivity between $d_{i'}$ and the next real boundary d_{i+1} is identical to that of the layer beyond d_{i+1}, denoted as R_{i+1}. This virtual boundary is then progressively moved away from its original position, and the corresponding change in the tool response, ΔF, is computed after each step. As the virtual boundary recedes, ΔF gradually diminishes. The distance from the tool to the virtual boundary at the moment ΔF first falls to a preset detection threshold Thr, which is defined as the equivalent DOD within the given multi-layer context.

To illustrate, consider a seven-layer model with layer thicknesses of 1.0, 1.5, 2.5, 1.5, 2.0, 2.5, and 1.0 m, and resistivities of 20, 2, 20, 2, 20, 2, and 20 Ω·m. The relative dip angle between the tool and the formation is 80°. The model includes six boundaries and seven resistivity values. Assuming a noise standard deviation of 0.04 for both Att and PS measurements, we analyze a measurement point at a vertical depth of 2.3 m—located in the second layer and near the second boundary (marked by a black box in Fig. 6(c)). Fig. 6(a) shows the elements of the Fisher information matrix. Its diagonal elements indicate the information content of each parameter. A prominent peak is observed for the parameters corresponding to d_2 and the resistivity R_1, confirming that the measurements are most sensitive to the nearest boundary and its host layer resistivity, as theoretically expected. Using the L_2-norm of the normalized Jacobian matrix to define parameter sensitivity and setting a relative sensitivity threshold of 1% (Fig. 6(b)), the sensitivities for d_1, d_2, d_3, R_0, R_1, R_2, and R_3 exceed the threshold. In contrast, parameters associated with distant boundaries and layers fall below the threshold, indicating that they cannot be reliably estimated. The uncertainty of the estimable boundary positions is represented by error bars in the black box in Fig. 6(c). The uncertainty ranges are 1 ± 0.057 m for d_1, 2.5 ± 0.010 m for d_2, and 5 ± 0.283 m for d_3. Fig. 6(c) also plots the estimated uncertainty ranges for each detectable boundary as the tool moves through the formation (black pentagram indicates tool position). In this model, the tool can resolve up to four boundaries, with uncertainty increasing as the distance to the boundary grows.

Table 2 presents the computed equivalent DOD above and below the tool at various vertical depths within the seven-layer model. These values are obtained by applying the threshold-based detection criterion to a virtual boundary. This table illustrates how the detection range varies with tool position in a multi-boundary environment, demonstrating that the DOD depends not only on resistivity contrast but also on the specific layer configuration encountered.

To verify the consistency between the FIM framework and the Monte Carlo approach presented in Section 2.1, we apply the same analysis to the single-boundary model. Under identical conditions (resistivities of 10 and 1 Ω·m, SNR = 40 dB), when the tool-to-boundary distance is 2.99 m, the CRLB gives a theoretical

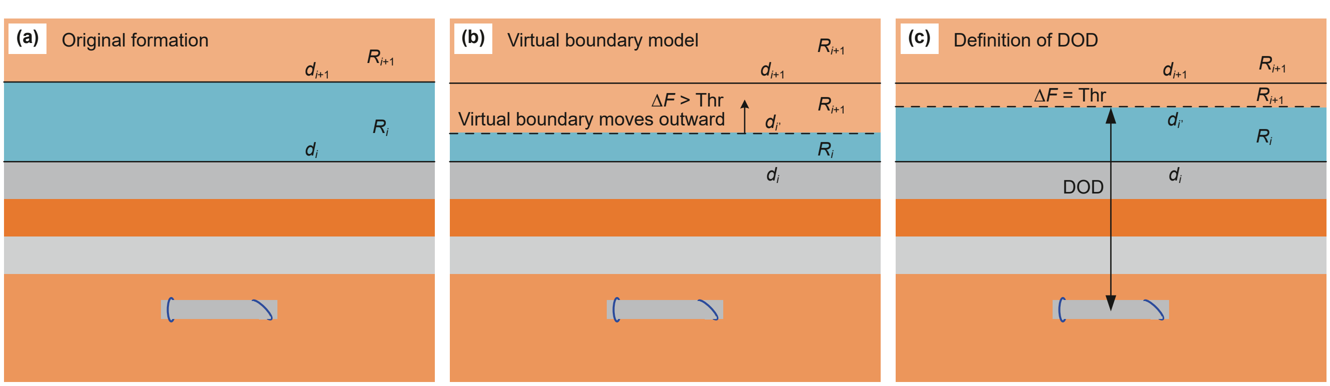

Fig. 5. Schematic definition of DOD in a multi-layer formation model.

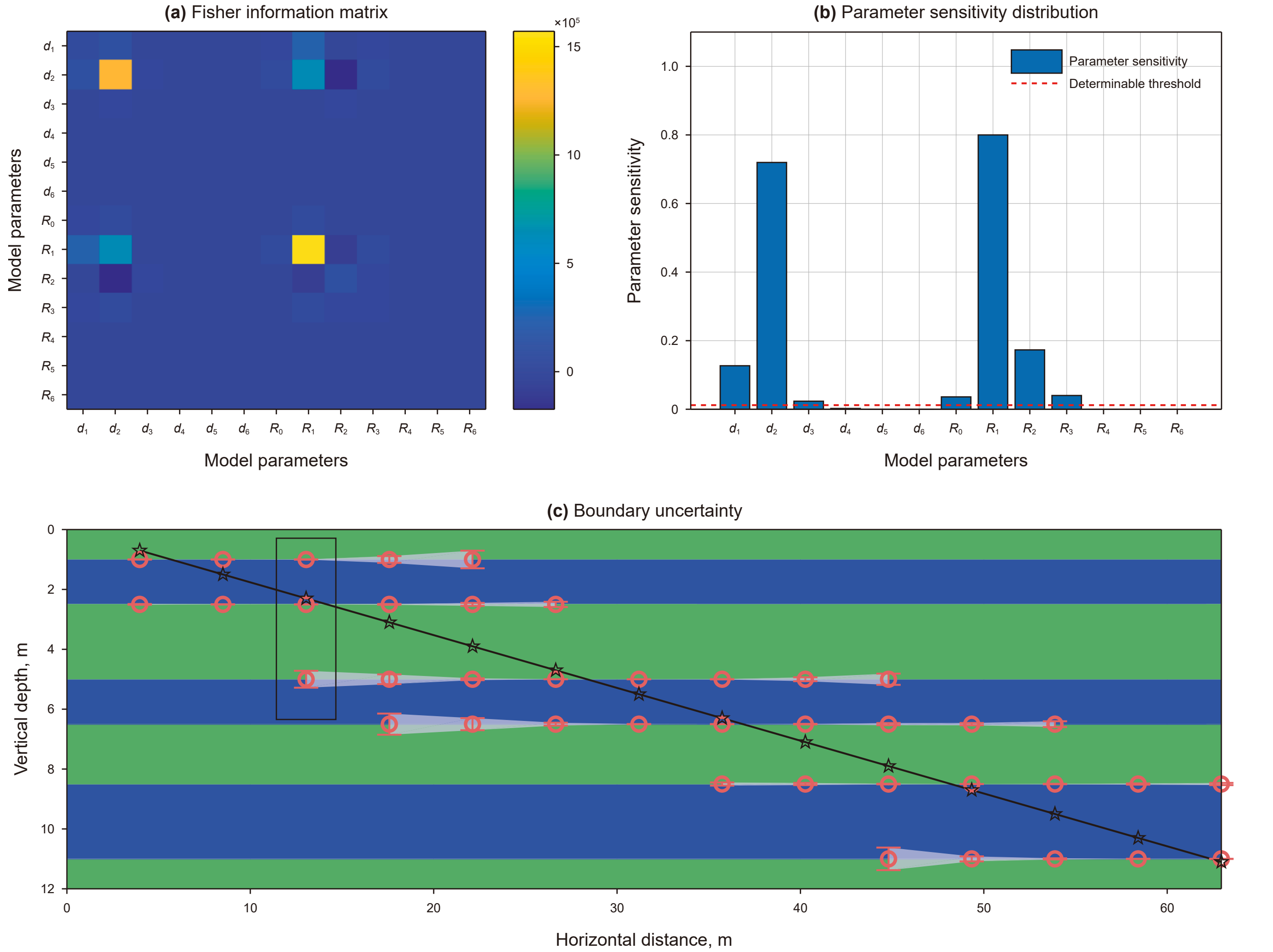

Fig. 6. Fisher information matrix analysis for a seven-layer model: **(a)** Fisher information matrix elements; **(b)** parameter sensitivity distribution; **(c)** boundary uncertainty and tool position.

Table 2
Equivalent DOD for the seven-layer model at different measurement positions.

Measurement sequence	Vertical depth, m	DOD above the tool, m	DOD below the tool, m
1	0.7	2.5	3.9
2	1.5	2.3	3.8
3	2.3	2.8	3.6
4	3.1	2.5	3.4
5	3.9	2.7	3.4
6	4.7	2.4	2.6
7	5.5	3.1	3.1
8	6.3	2.8	2.4
9	7.1	2.5	2.5
10	7.9	2.3	3.0
11	8.7	2.5	2.6
12	9.5	3.5	3.1
13	10.3	3.7	2.3
14	11.1	3.8	2.7

standard deviation of 0.064 m for the boundary position. This corresponds to a 95% confidence interval of [2.862, 3.118] m (uncertainty range = 0.256 m), which closely matches the Monte-Carlo-based uncertainty range of 0.28 m shown in Fig. 3. This agreement confirms that the FIM/CRLB theory correctly captures the estimation-accuracy limit even for the simplest model, and its predictions are consistent with statistically derived detection-probability ranges near the detection limit.

2.3. Multi-boundary detection capability

To determine how many formation boundaries AETs can interpret, a series of representative formation cases are analyzed using the Fisher information matrix. An integrated formation model (blue curve in Fig. 7(a)) was constructed, with layer thicknesses ranging from 0.6 m to 8.0 m and resistivities spanning 0.2 Ω·m to 200 Ω·m. The model incorporates typical geological features such as coarsening-upward and fining-upward sequences, massive beds, and thin intercalations. Latin hypercube sampling was employed to capture a wide range of formation scenarios likely encountered in actual drilling operations. The tool configurations were used: a resistivity measurement with 0.711 m and 1.02 m spacings at 2 MHz, and geosignals with 0.864 m and 2.44 m spacings at 100 kHz and 400 kHz. All simulations assumed a well inclination of 85°.

The apparent resistivity responses are shown in Fig. 7(a). The PS apparent resistivity exhibits superior vertical resolution for thin beds compared to the Att apparent resistivity response. Analysis of the geosignal response (Fig. 7(b)) further shows that the short-

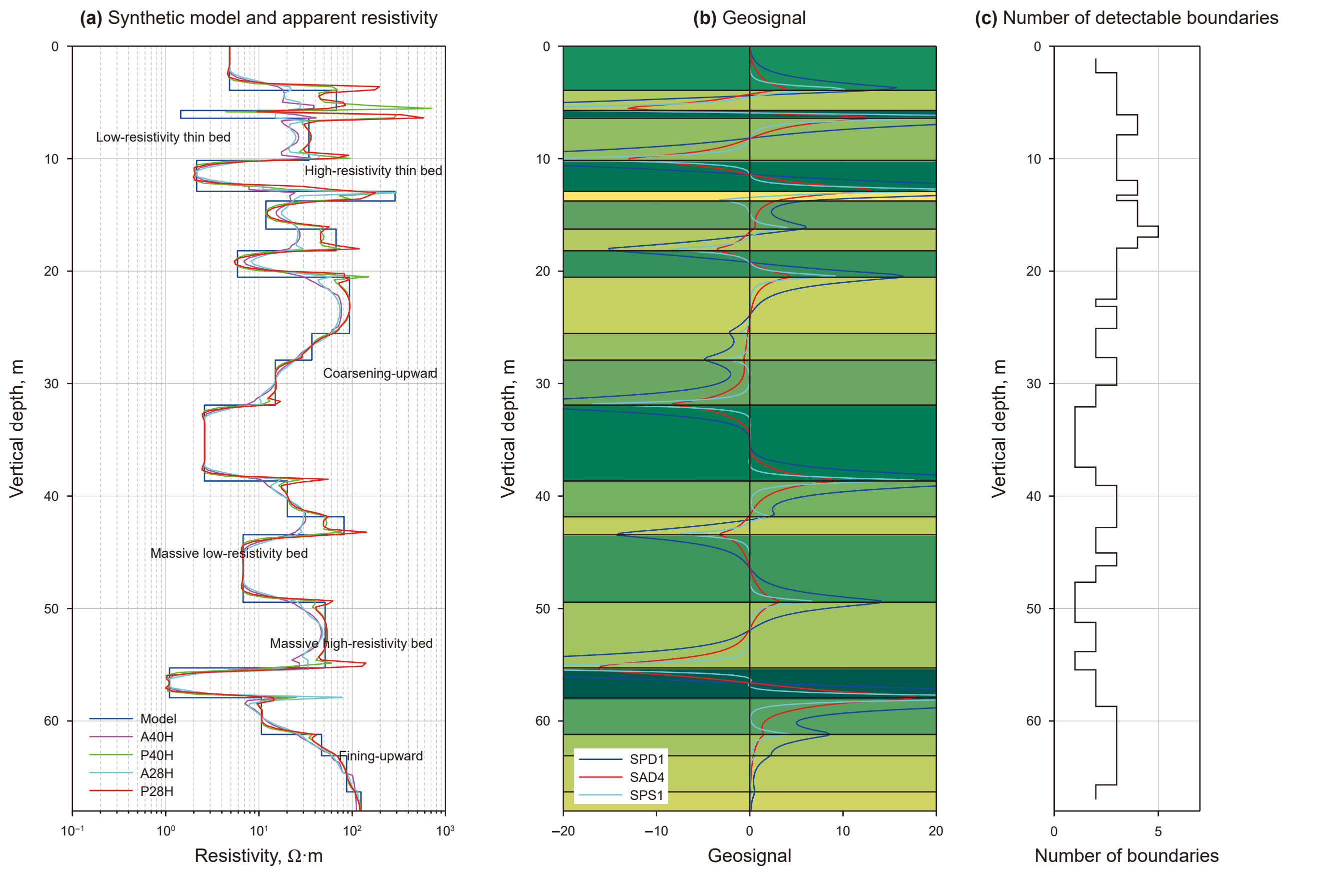

Fig. 7. Characterization of multi-boundary detection capability: **(a)** synthetic model and apparent resistivity; **(b)** geosignal; **(c)** the maximum number of detectable boundaries.

spacing PS geosignal provides exceptional resolution, clearly delineating both thin-bed boundaries and transitional boundaries in cyclic sequences. The Fisher information matrix framework was applied to quantify the tool's practical detection capability in this model. For each measurement point, the maximum number of reliably detectable boundaries was computed. Fig. 7(c) demonstrates that the tool can detect up to five boundaries simultaneously in thin-bedded intervals, while the detectable number predominantly ranges from 1 to 4 in other sections.

To examine the distribution of detectable boundaries in further detail, a separate statistical analysis was performed on the number of boundaries above and below the tool. Results from Fig. 8(a) show that the total number of detectable boundaries is predominantly 2 to 3. In Fig. 8(b), the first number on the horizontal axis indicates the number

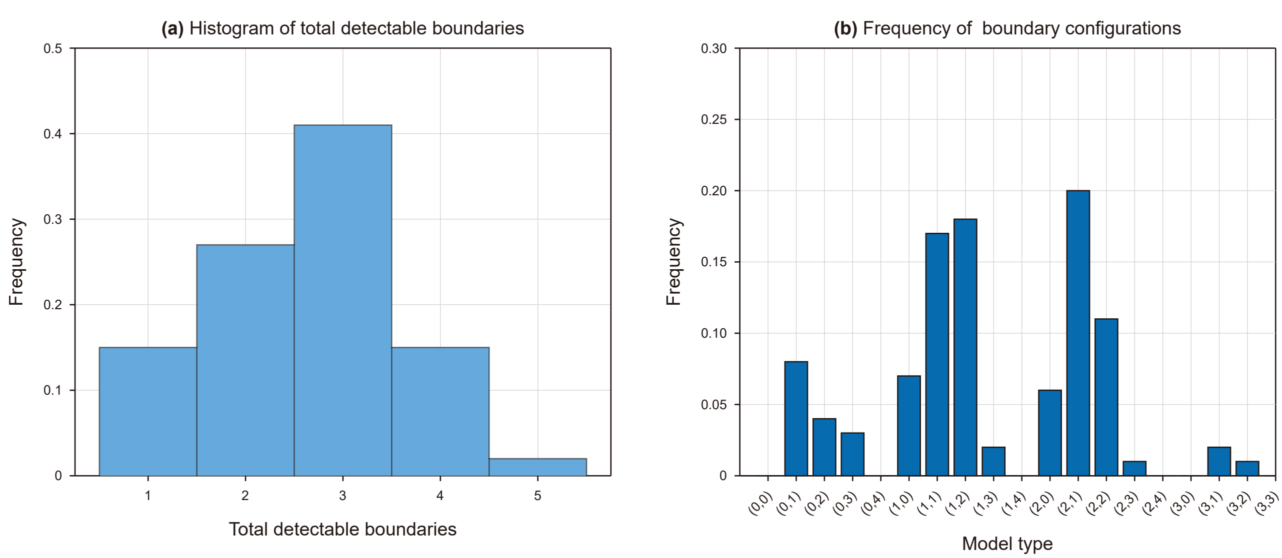

Fig. 8. Statistical analysis of detection boundaries: **(a)** histogram of total detectable boundaries; **(b)** frequency of boundary configurations.

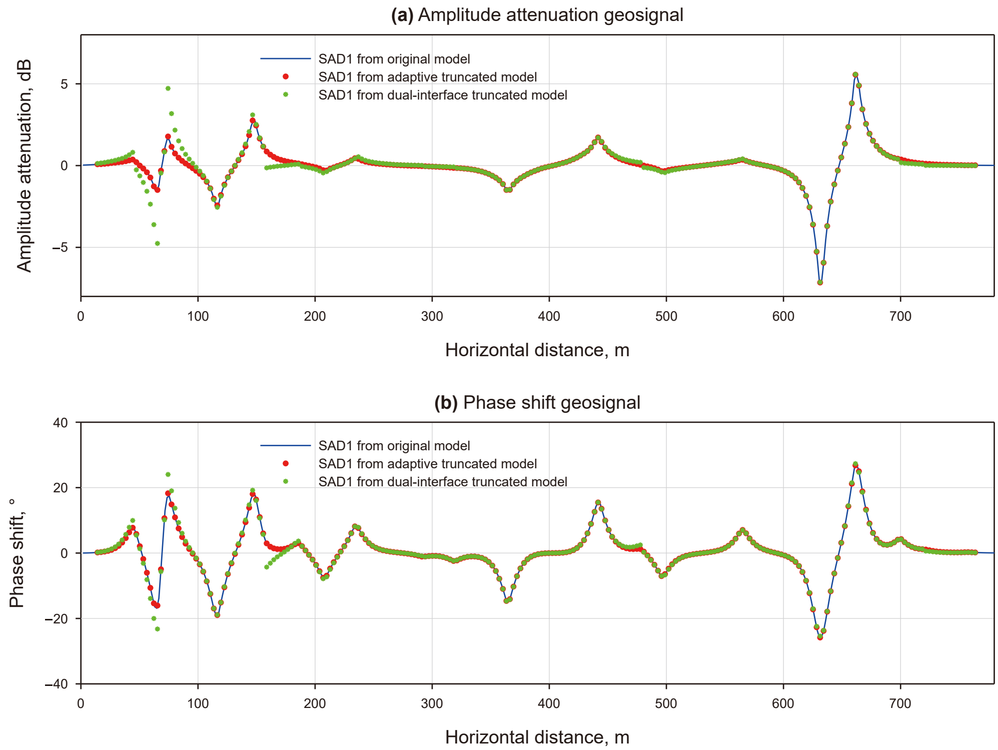

Fig. 9. Comparison of geosignal of the original model (blue), adaptive truncated model (red), and two-boundary truncated model (green): **(a)** Att geosignal; **(b)** PS geosignal.

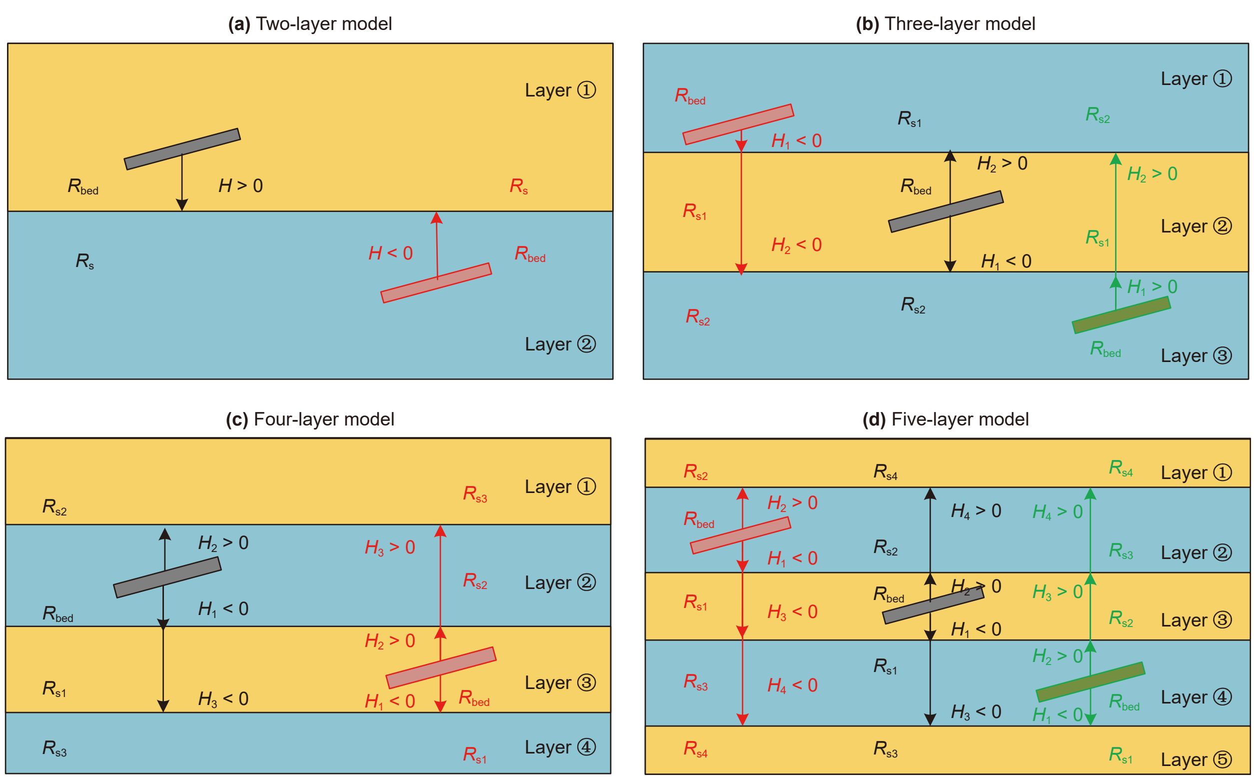

Fig. 10. Inversion models: **(a)** two-layer model; **(b)** three-layer model; **(c)** four-layer model; **(d)** five-layer model.

of detectable boundaries below the tool, while the second number corresponds to those above it. These statistics provide a practical basis for defining the number of boundaries in the inversion model.

To validate the boundary detection analysis, forward responses were compared among three models: the full original model, an adaptive truncated model based on the multi-boundary detection assessment, and a two-boundary truncated model. As shown in

Table 3
Detailed parameters for each model.

Inversion model	Host layer	Model parameters
Two-layer model	Layer ①	R_{bed}, R_s, H (>0)
	Layer ②	R_{bed}, R_s, H (<0)
Three-layer model	Layer ①	R_{bed}, R_{s1}, H_1 (<0), R_{s2}, H_2 (<0)
	Layer ②	R_{bed}, R_{s1}, H_1 (<0), R_{s2}, H_2 (>0)
	Layer ③	R_{bed}, R_{s1}, H_1 (>0), R_{s2}, H_2 (>0)
Four-layer model	Layer ②	R_{bed}, R_{s1}, H_1 (<0), R_{s2}, H_2 (>0), R_{s3}, H_3 (<0),
	Layer ③	R_{bed}, R_{s1}, H_1 (<0), R_{s2}, H_2 (>0), R_{s3}, H_3 (>0)
Five-layer model	Layer ②	R_{bed}, R_{s1}, H_1 (<0), R_{s2}, H_2 (>0), R_{s3}, H_3 (<0), R_{s4}, H_4 (<0)
	Layer ③	R_{bed}, R_{s1}, H_1 (<0), R_{s2}, H_2 (>0), R_{s3}, H_3 (<0), R_{s4}, H_4 (>0)
	Layer ④	R_{bed}, R_{s1}, H_1 (<0), R_{s2}, H_2 (>0), R_{s3}, H_3 (>0), R_{s4}, H_4 (>0)

Note: R_{bed} represents the resistivity of the layer where the tool is located, while R_s represents the resistivity of the surrounding rock. H (>0) denotes the distance to the boundary above the tool, while H (<0) denotes the distance to the boundary below the tool.

Fig. 9, the geosignal of the adaptive truncated model closely matches the geosignal of the original model, confirming that boundaries beyond the tool's effective detection range have a negligible impact. In contrast, the response of the two-boundary model shows significant deviations in thin layers, underscoring the limitations of the traditional two-boundary assumption in complex formations.

3. Trans-layer inversion methodology

3.1. Construction of inversion model library

Based on a comprehensive analysis of the tool's multi-boundary detection capabilities, we have established multiple inversion models ranging from two-layer to five-layer configurations. These models adequately represent the vast majority of formation conditions encountered in actual drilling operations. Simultaneously, we have fully accounted for the relative position of the tool within the formation to avoid the introduction of additional parameters. As illustrated in Fig. 10, the instrument in two- and five-layer models may be situated in any layer. Detailed parameters for each model are provided in Table 3. It is noteworthy that, compared to the conventional three-layer model typically assuming a central tool position, the model library incorporates scenarios with the tool located in any layer. This refinement significantly enhances the adaptability of three-layer inversion to varying tool-formation relative positions, thereby improving the stability and reliability of inversion results.

3.2. Gradient algorithms and model initialization

The inversion of azimuthal electromagnetic measurements is, in essence, an optimization process that seeks the model parameters by minimizing the misfit between predicted and actual measurements. The formulation of the objective function is critical, as it directly governs inversion accuracy and algorithmic stability. This paper employs a unified objective function based on the L_2-norm of the residuals between forward modeling data $S(\mathbf{m})$ and measured data $\mathbf{d}^{obs}$:

$$\min \boldsymbol{\Phi} = \left(S(\mathbf{m}) - \mathbf{d}^{obs}\right)\mathbf{W}_d\left(S(\mathbf{m}) - \mathbf{d}^{obs}\right)^T + \lambda\left(\mathbf{m} - \mathbf{m}_{ref}\right)\mathbf{W}_m\left(\mathbf{m} - \mathbf{m}_{ref}\right)^T, \tag{10}$$

where $\mathbf{m}$ is the parameter vector defining the model, $\mathbf{W}_d$ and $\mathbf{W}_m$ are weight matrices for measured data and model parameters, respectively, and λ is the regularization parameter. The reference model $\mathbf{m}_{ref}$ can be derived from previous inversion results or geological continuity constraints. This regularization term mitigates noise, addresses ill-posedness, and incorporates prior knowledge to enhance solution stability.

The Levenberg-Marquardt (L-M) algorithm (Marquardt, 1963) is widely used in optimization due to its second-order convergence rate. It incorporates a damping factor μ to regulate the step size and search direction. The parameter update rule is given by:

$$\mathbf{m}_{k+1} = \mathbf{m}_k - \frac{\mathbf{W}_d \cdot \mathbf{J}^T(\mathbf{m})\left(S(\mathbf{m}) - \mathbf{d}^{obs}\right) \cdot \mathbf{W}_d{}^T - \lambda \mathbf{W}_m \cdot \mathbf{W}_m{}^T\left(\mathbf{m} - \mathbf{m}_{ref}\right)}{\mathbf{W}_d \cdot \mathbf{J}^T(\mathbf{m}) \cdot \mathbf{J}(\mathbf{m}) \cdot \mathbf{W}_d{}^T + \lambda \mathbf{W}_m \cdot \mathbf{W}_m{}^T + \mu \mathbf{I}}, \tag{11}$$

where $\boldsymbol{J}(\mathbf{m})$ denotes the Jacobian matrix of the forward model with respect to the parameters.

The regularization parameter λ is determined following Pardo and Torres-Verdín (2015) as:

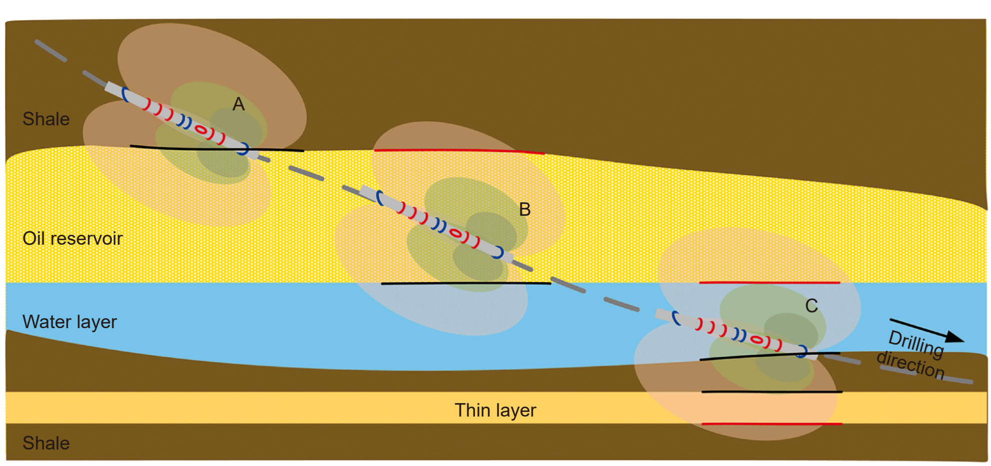

Fig. 11. Schematic diagram of multi-layer initial model generation.

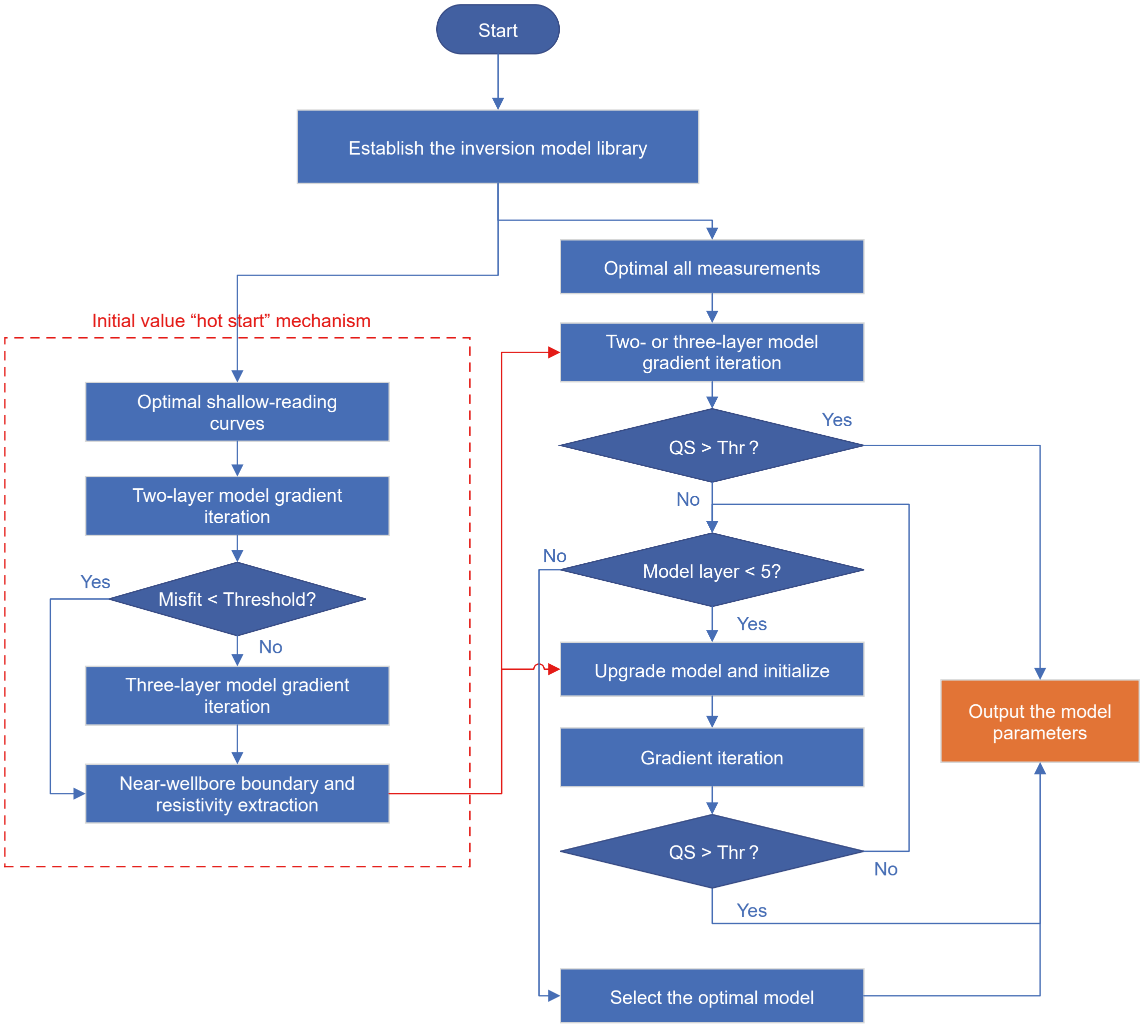

Fig. 12. Simplified workflow of the adaptive trans-layer inversion. The "hot-start" uses shallow-reading curves, while final optimization employs all available measurements.

$$\lambda_k = 0.1 \times \frac{\left\| \mathbf{W}_\mathrm{d}\left(\mathrm{S}(\mathbf{m}) - \mathbf{d}^{\mathrm{obs}}\right) + \mathbf{J}(\mathbf{m})\Delta\mathbf{m} \right\|_2^2}{\left\| \mathbf{m} - \mathbf{m}_{\mathrm{ref}} \right\|_2^2} \tag{12}$$

Here, the damping factor μ is adjusted adaptively based on the ratio ρ of the actual to the predicted reduction in the residual:

$$\rho = \frac{\boldsymbol{\Phi}(\mathbf{m}_k) - \boldsymbol{\Phi}(\mathbf{m}_{k+1})}{\Delta\mathbf{m}^\mathrm{T}\left(\mathbf{J}^\mathrm{T}\mathbf{W}_\mathrm{d}\left(\mathrm{S}(\mathbf{m}_k) - \mathbf{d}^{\mathrm{obs}}\right)\right) + \frac{1}{2}\Delta\mathbf{m}^\mathrm{T}\left(\mathbf{J}^\mathrm{T}\mathbf{J} + \mu_k\mathbf{I}\right)\Delta\mathbf{m}} \tag{13}$$

$$\mu_{k+1} = \begin{cases} \mu_k \times 0.5, \ \rho > 0.75 \\ \mu_k \times 2, \ \rho < 0.25 \\ \mu_k, \quad \text{otherwise} \end{cases} . \tag{14}$$

This strategy increases μ to stabilize convergence when far from the optimum and decreases μ to accelerate convergence when approaching it.

Although the L-M algorithm offers fast local convergence, this comes at the cost of a high dependency on the quality of the initial model. This dependency is even more critical for multi-layer inversion, where the severe non-uniqueness of the problem makes the choice of initial parameters particularly consequential. To overcome this limitation, we introduce a hierarchical hot-start initialization strategy that leverages robust results from shallow-reading inversion to structurally constrain more complex multi-layer models. As illustrated in Fig. 11, black boundaries are those

Table 4
Input measurements for the trans-layer inversion workflow.

Curve type	Measurement mode	Spacing	Frequency
Shallow-reading	Resistivity mode	0.41 m 0.56 m	2 MHz
	Geosignals mode	0.56 m	400 kHz 2 MHz
Deep-reading	Resistivity mode	0.71 m 0.86 m 1.02 m	2 MHz
	Geosignals mode	2.44 m 2.13 m 0.86 m	400 kHz, 100 kHz

identified by shallow-reading curves, while red boundaries are extensions detected by deep-reading curves. The inversion process begins with two- or three-layer model inversion derived from shallow-reading curves. When the model complexity is increased from a k-layer to a $(k+1)$-layer configuration, the initial parameter vector $\mathbf{m}_{\text{init}}^{(k+1)}$ is constructed as:

$$\mathbf{m}_{\text{init}}^{(k+1)} = \left[\mathbf{m}_{\text{opt}}^{(k)}, \mathbf{p}_{\text{new}}\right] \tag{15}$$

where $\mathbf{m}_{\text{opt}}^{(k)}$ is the converged solution from the k-layer model inversion, and $\mathbf{p}_{\text{new}}$ represents the parameters for the newly introduced layer. The signs of the distance parameters in $\mathbf{p}_{\text{new}}$ are determined during model upgrade by evaluating two competing structural hypotheses—adding a boundary above or below the tool—and selecting the one that yields a better fit to the measurement data. The hypothesis with the lower data misfit is chosen, defining the sign of H according to the convention in Table 3.

This initialization is then further refined by incorporating spatial continuity, empirical resistivity ranges, and physical detection limits, following three constraint principles:

(1) Set resistivity bounds for each layer using regional geology or offset well data. Initialize the host layer resistivity from the apparent resistivity curve, and randomly generate adjacent layer resistivities within ranges consistent with expected contrasts.
(2) Confine initial boundaries to the tool's effective detection range, calculated from the current resistivity model, to avoid non-physical solutions.
(3) Leverage lateral continuity by using optimal parameters from adjacent depth points as a reference. Apply normally distributed perturbations to this reference to generate an ensemble of initial models, embedding spatial prior information.

To balance global convergence robustness with computational efficiency, a controlled strategy for generating initial models is implemented. Maximum limits are set for the number of initial models per complexity level: 16 for two-layer, 24 for three-layer, 50 for four-layer, and 80 for five-layer configurations. Additionally, when leveraging lateral formation continuity, 10 initial models are generated by perturbing the reference model from adjacent depth points. These limits, determined through extensive preliminary numerical experiments, ensure sufficient sampling of the parameter space to mitigate convergence to local minima while imposing a strict upper bound on the computational overhead per depth point.

3.3. Trans-layer inversion workflow

To achieve adaptive selection of inversion model complexity while balancing computational efficiency and accuracy, we design an adaptive trans-layer inversion workflow and introduces a comprehensive quality score (QS) as the criterion for model selection. The QS combines a reward for data fit with a penalty for model complexity, defined as follows:

$$\text{QS} = \omega_1 \cdot \mathrm{e}^{\left(-\frac{\left\|S(\mathbf{m})-\mathrm{d}^{\text{obs}}\right\|_2^2}{\tau}\right)} + \omega_2 \cdot \left(1 - \frac{N_{\text{params}} - 3}{9}\right) \tag{16}$$

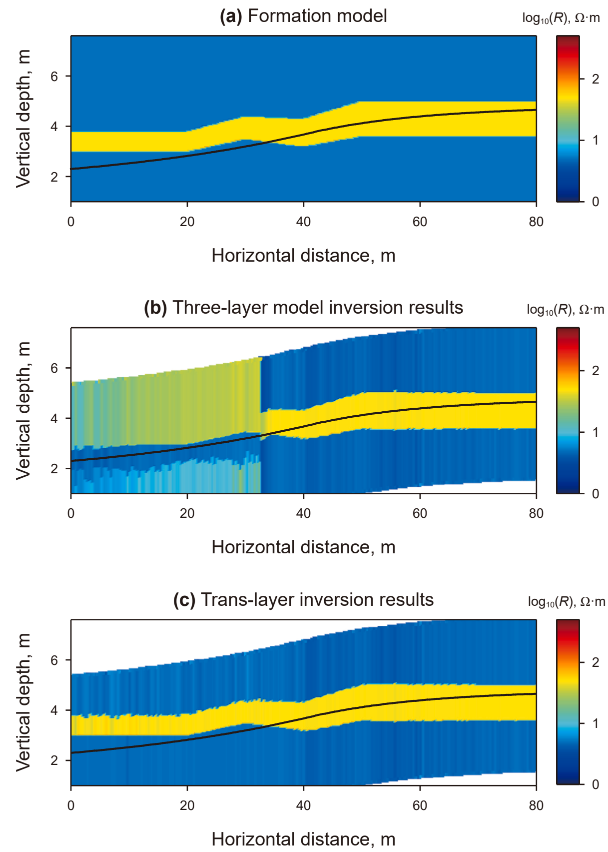

Fig. 13. Comparison of inversion results for the three-layer sand-shale model: **(a)** formation model; **(b)** traditional three-layer model inversion results; **(c)** adaptive trans-layer inversion results.

where ω_1, ω_2 are weighting coefficients, satisfying $\sum \omega_i = 1$, τ is a normalization factor, and N_{params} is the number of parameters in the current inversion model. The first term rewards a lower residual sum of squares between the forward model response and measured data, while the second term penalizes higher model complexity. The QS ranges from 0 to 1, with higher values indicating better overall inversion quality. Fig. 12 illustrates the adaptive trans-layer inversion workflow based on the QS. Initially, a model library spanning from two to five layers is established. Shallow-reading curves are first inverted using a two- or three-layer model. Multiple initial models are optimized through gradient iteration to resolve the near-wellbore boundaries and resistivity distribution. This result provides the "hot-start" initial model for the subsequent step. The model is then optimized using the complete set of measurements (all shallow- and deep-reading curves as listed in Table 4). If the QS meets the threshold, the result is accepted and output. Otherwise, the model complexity is incremented by adding a boundary, with parameters inherited from the previous model under strong constraints for further gradient-based optimization. The model with a QS exceeding the threshold is selected as optimal. If no model meets the threshold, the one with the highest QS is output. To leverage formation continuity and improve convergence, model parameters from adjacent inverted depth points are used as a reference model to constrain the initialization at the current depth.

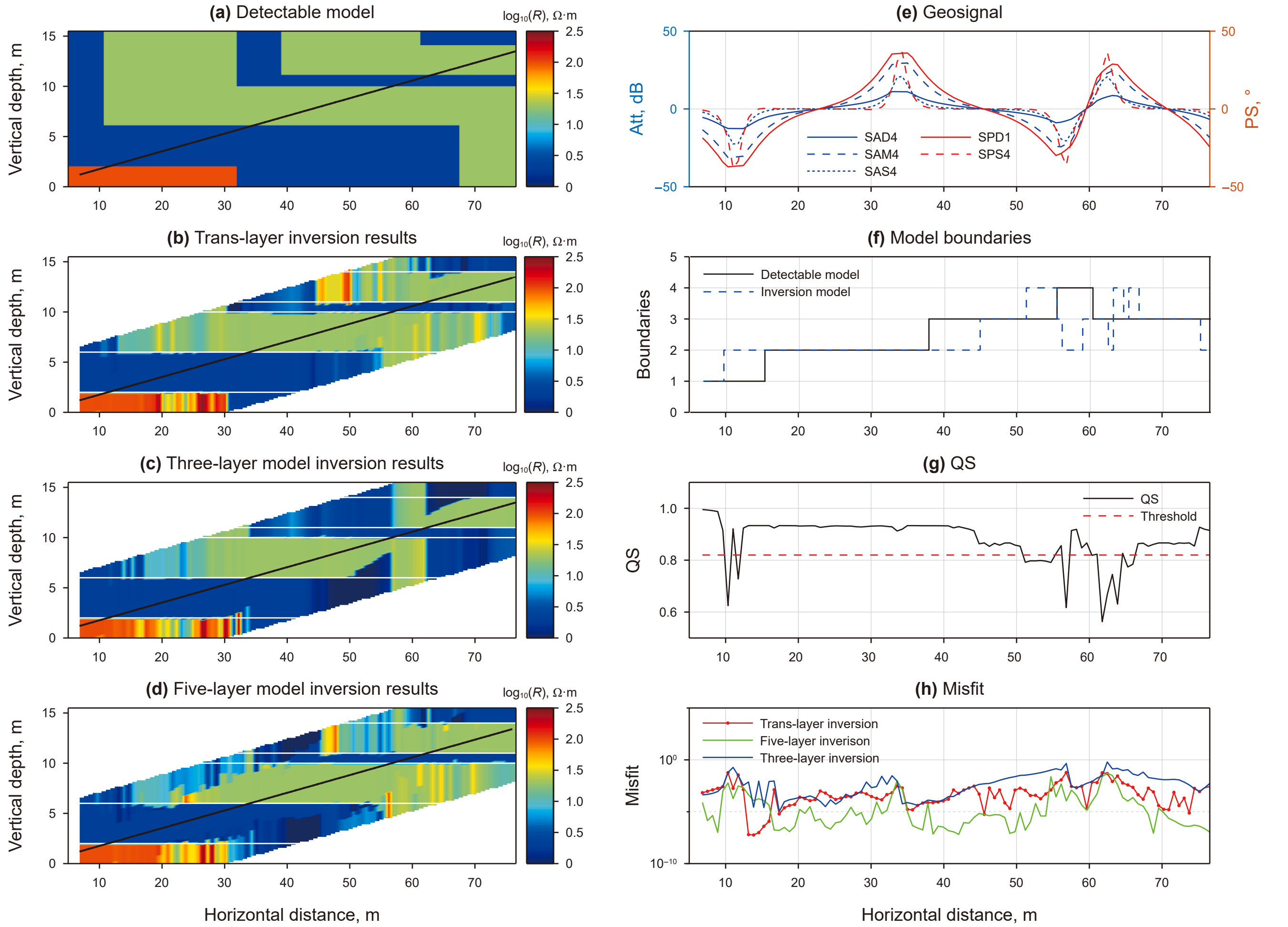

Fig. 14. Inversion performance comparison in a thin-layer formation: **(a)** the formation model truncated based on multi-boundary detection capability; **(b)** trans-layer inversion results; **(c)** three-layer model inversion results; **(d)** five-layer model inversion results; **(e)** corresponding geosignal responses; **(f)** comparison of the boundaries between detectable model and trans-layer inversion model; **(g)** variation of the quality factor (QS) with horizontal distance; **(h)** residual misfit comparison of the three inversion results.

4. Numerical and field examples

To systematically validate the correctness, stability, and engineering applicability of the proposed adaptive inversion method, three synthetic examples and one field case were designed and conducted. All experiments used the same tool parameters and computational platform. The input measurements for the trans-layer inversion are listed in Table 4. Through extensive numerical testing, the weight coefficients for the residual misfit and model complexity in the QS were set to 0.7 and 0.3, respectively, with the model upgrade threshold at 0.82. Inversion computations were performed point-by-point on a computer equipped with an Intel i7-13700 K processor and 64 GB of RAM.

4.1. *Case study I: validation of basic correctness and algorithm stability*

To examine the fundamental performance of the trans-layer inversion method, a three-layer sand-shale sequence model shown in Fig. 13(a) was constructed, with a sandstone resistivity of 20 Ω·m and overlying/underlying shale resistivities of 2 Ω·m. Sandstone thickness varied from 0.8 m to 1.5 m, and the formation dip angle changed between 85° and 90° to simulate realistic geological conditions. A 5% Gaussian noise was added to the

Table 5
Inversion results statistics.

Inversion model	Mean square error	Average inversion time
Three-layer model	0.0303	2 s
Five-layer mode	0.0017	19 s
Trans-layer model	0.0040	9 s

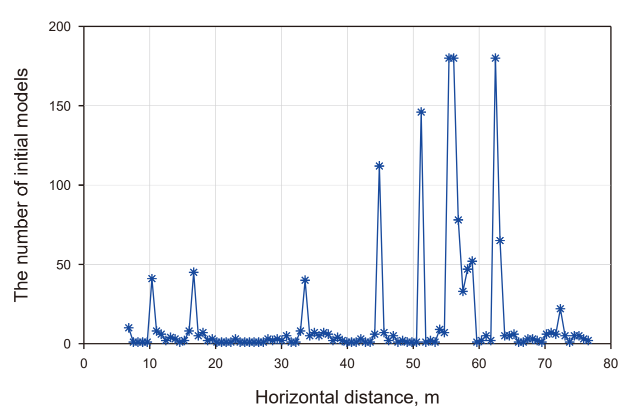

Fig. 15. The number of initial guesses used when the tool is located at different recording position.

forward responses to simulate measurement errors. Fig. 13(b) shows the inversion results from the traditional three-layer model. Before the tool entered the sandstone layer (horizontal distance <32 m), limited by the model structure, only the lower boundary of the upper sandstone could be identified. In contrast, the proposed trans-layer inversion method not only accurately reconstructed the upper and lower boundaries and resistivity distribution (Fig. 13(c)) but also improved computational efficiency by approximately 20% compared to the traditional method, owing to the effective use of lateral continuity constraints. This example illustrates that the trans-layer inversion method provides higher resolution, a capability attributed to its comprehensive model library, thereby permitting the detection of reservoir structures prior to tool entry.

4.2. Case study II: comparison of accuracy and efficiency in thin-bed environments

To evaluate the comprehensive performance of the method in thin-bed environments, a six-layer geological model was established. The layer thicknesses from top to bottom were 2.0, 4.0, 4.0, 1.0, 3.0, and 1.5 m, with corresponding resistivities of 100, 2, 20, 2, 20, and 2 Ω·m. The forward responses were simulated at an inclination angle of 80°, and inversions were performed using the trans-layer method, with fixed three- and five-layer inversions also run for comparison.

Fig. 14(a) shows the formation model truncated according to the tool's multi-boundary detection capability, and Fig. 14(e) displays the corresponding geosignal responses. The inversion results (Fig. 14(b)–(d)) show that the trans-layer inversion results generally match the truncated model well. In contrast, the traditional three-layer inversion exhibits significant distortion at distant boundaries in the 50–70 m interval, influenced by the low-resistivity thin layer. While the fixed five-layer inversion identifies nearby thin beds, it shows overfitting in the thick-bed section at 23–33 m. Fig. 14(f) compares the number of detectable boundaries at each measurement point with the number of boundaries selected by the trans-layer inversion method, showing generally consistent trends. Notably, the number of boundaries selected occasionally exceeds the local theoretically detectable number. This can be attributed to two key mechanisms: (1) In high-angle/horizontal wells, traversing thin beds often generates "horn" features in the response, which temporarily increase the local misfit. A model with a slightly higher layer count can sometimes represent the smoother overall signal trend more effectively. If the resulting misfit reduction outweighs the QS penalty for added complexity, the algorithm selects this model. (2) The inversion incorporates spatial continuity as a constraint, enabling the model to retain a "memory" of boundaries identified at neighboring depth points—even when local FIM analysis alone lacks sufficient information for independent resolution. This continuity constraint enhances the lateral stability and geological consistency of the interpreted section. Fig. 14(g) shows the variation of the QS factor with horizontal distance, where a temporary decrease in QS is observed when crossing the boundary due to "horn" responses. Fig. 14(h) compares the misfit of the three results, and Table 5 summarizes the overall performance: the fixed three-layer model inversion has a mean square error of 0.0303 and an average processing time of 2 s per point; the fixed five-layer model inversion reduces the error to 0.0017 but increases the time to 19 s; the adaptive trans-layer inversion achieves an error of 0.004 with only 9 s processing time. By avoiding unnecessarily complex models, the adaptive trans-layer inversion method achieved a better balance between accuracy and efficiency.

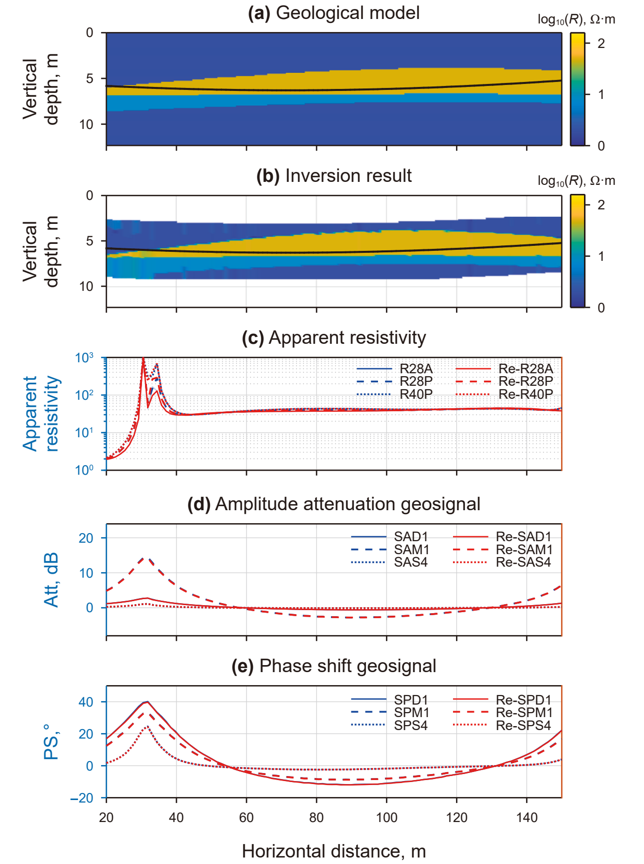

Fig. 16. Reservoir structure and oil-water contact identification via trans-layer inversion: **(a)** formation model; **(b)** trans-layer inversion results; **(c)** apparent resistivity responses; **(d)** Att geosignals; **(e)** PS geosignals.

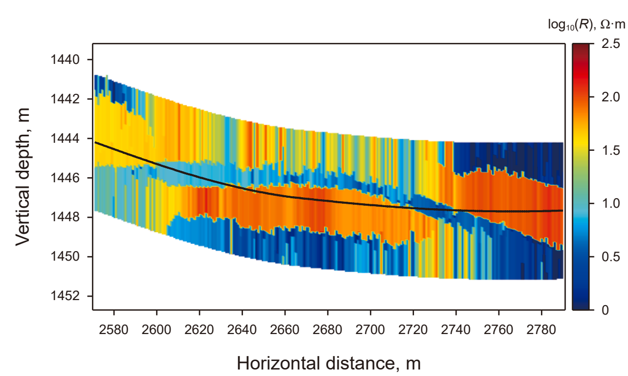

Fig. 17. Field example of trans-layer inversion results from Well A.

The practical efficiency of the adaptive trans-layer inversion is further illuminated by analyzing the number of initial models evaluated per depth point. Fig. 15 illustrates the cumulative count of initial models used during the inversion of the six-layer model. The results demonstrate that for the majority of the sampling depth, the algorithm requires fewer than 10 initial models to converge. This high efficiency is attributed to the spatial continuity constraints, which provide strong priors that drastically reduce the need for blind exploration. Only when the tool traverses thin-bed boundaries (e.g., within the 55–63 m interval), where the geosignal exhibits rapid "horn" features and convergence is more challenging, does the algorithm utilize a larger portion of the available initial models to ensure robustness. This adaptive consumption of computational resources underscores the method's ability to dynamically allocate effort where it is most needed, contributing directly to the favorable balance between accuracy and speed reported in Table 5.

4.3. Case study III: validation of oil-water contact identification in an anticlinal reservoir model

This example simulates a typical geosteering scenario in an anticlinal reservoir, aiming to validate the comprehensive capability of the proposed method in simultaneously identifying structural boundaries and fluid contacts. As shown in Fig. 16(a), the geological model consists of upper and lower shale caprocks (resistivity 2 Ω·m) and a central sandstone reservoir. An oil-water contact exists within the reservoir, with the overlying oil zone having a resistivity of 50 Ω·m and the underlying water zone 8 Ω·m. The well trajectory (black curve in the figure) traverses this anticlinal structure in a near-horizontal manner.

Applying the proposed trans-layer inversion method yields the resistivity curtain plot shown in Fig. 16(b). The results demonstrate that the method not only accurately delineates the structural top and bottom boundaries of the reservoir but also clearly reveals the position of the internal oil-water contact. The inverted resistivity curtain effectively distinguishes the high-resistivity oil zone from the low-resistivity water zone, showing a high degree of spatial consistency with the true model. This example highlights the method's potential in complex reservoirs, ensuring accurate wellbore placement within the productive sweet spot and helping avoid early water influx.

4.4. Field case study: application in a complex reservoir

To further validate the practical applicability of the proposed trans-layer inversion method, we applied it to field data acquired from Well A drilled through a complex clastic reservoir. The inversion results are presented as a resistivity curtain plot in Fig. 17. The trans-layer inversion results clearly delineate a thin shale layer developed within the target zone. Notably, across most of the logged interval, the method successfully recovers both the top and bottom boundaries of this thin conductive layer simultaneously. The trajectory initially approaches the reservoir from below, maintains position near the reservoir top, and subsequently penetrates upward through the thin low-resistivity bed before re-entering the thick reservoir section above. The application of trans-layer inversion technology significantly improves the reservoir target intersection rate and provides critical data support for refining reservoir characterization and optimizing development plans.

5. Conclusions

To overcome the trade-off between accuracy and efficiency inherent in traditional fixed-layer inversion methods for azimuthal electromagnetic measurements, this study systematically assessed AETs' multi-boundary detection capability, constructed an inversion model library, and developed an adaptive trans-layer inversion methodology. The main conclusions are as follows:

(1) A quantitative characterization method for multi-boundary detection capability was established based on the Fisher information matrix. Analysis results indicate that the AET can typically detect two to four boundaries. Forward modeling confirms that boundaries outside the effective detection range contribute negligibly to the tool response, thereby validating the rationality and accuracy of the quantitative characterization method.

(2) The inversion model library constructed in this study covers a wide range of practical detection scenarios. Its structural diversity significantly enhances the algorithm's adaptability to dynamically varying formations.

(3) Compared to fixed-layer model inversion, the proposed trans-layer inversion method achieves a 91.5% reduction in mean square error relative to the three-layer inversion while doubling the computational efficiency of the five-layer inversion. It also delivers significantly improved resolution in thin-bed imaging, effectively resolving the inherent trade-off between accuracy loss from structural mismatch and efficiency degradation due to over-parameterization.

(4) Validation with field data from a complex clastic reservoir confirms the method's practical applicability. The trans-layer inversion successfully delineates a thin shale layer within the target zone, recovering both its top and bottom boundaries simultaneously, and provides critical guidance for well trajectory optimization.

Numerical tests and field validation collectively demonstrate the method's effectiveness. By adaptively selecting model complexity, the proposed framework achieves an optimal balance between accuracy and efficiency, offering a reliable solution for high-precision multi-boundary inversion in azimuthal electromagnetic LWD and supporting the intelligent interpretation of complex reservoirs.

CRediT authorship contribution statement

Yan-Xue Wang: Writing – original draft, Validation, Methodology, Conceptualization. **Lei Wang:** Supervision, Funding acquisition, Conceptualization. **Xin-Min Ge:** Writing – review & editing, Supervision. **Yi-Ren Fan:** Supervision, Funding acquisition.

Declaration of competing interest

The authors declare that they have no known competing financial interests or personal relationships that could have appeared to influence the work reported in this paper.

Acknowledgements

This research has been co-funded by the Oil & Gas Major Project of China, Grant Nos. 2025ZD1402102-05 and 2025ZD1401105-02; National Natural Science Foundation of China, Grant Nos. 42474152 and U23B2086; Shandong Provincial Natural Science Foundation, Grant No. ZR2023MD053.

References

Beer, R., Dias, L., da, Cunha, et al., 2010. Geosteering and/or reservoir characterization the prowess of new-generation LWD tools. In: SPWLA 51th Annual Logging Symposium. SPWLA-2010-93320.

Bittar, M., Klein, J., Beste, R., et al., 2009. A new azimuthal deep-reading resistivity tool for geosteering and advanced formation evaluation. SPE Reservoir Eval. Eng 12 (2), 270–279. https://doi.org/10.2118/109971-PA.

Ciabarri, F., Tarchiani, C., Alberelli, G., et al., 2023. Real-time rock-properties estimation for geosteering: Statistical rock-physics-driven inversion of seismic acoustic impedance and LWD ultradeep azimuthal resistivity. SPE Reservoir Eval. Eng 26 (4), 1224–1241. https://doi.org/10.2118/214407-PA.

Dupuis, C., Denichou, J., 2015. Automatic inversion of deep-directional-resistivity measurements for well placement and reservoir description. Lead. Edge 34 (5), 482–596. https://doi.org/10.1190/tle34050504.1.

Fischer, A., 2018. Fisher information and Cramér-Rao bound for unknown systematic errors. Measurement 113, 131–136. https://doi.org/10.1016/j.measurement.2017.08.042.

Hong, D.C., Chen, T., Ren, Q., et al., 2022. Foundation of ultradeep boundary detection based on the electric field characteristics. IEEE Trans. Geosci. Rem. Sens. 60, 1–11. https://doi.org/10.1109/TGRS.2021.3058990.

Hu, X.F., Fan, Y.R., Wu, F., et al., 2018. Fast multiple parameter inversion of azimuthal LWD electromagnetic measurement. Chin. J. Geophys. 61 (11), 4690–4701. https://doi.org/10.6038/cjg2018L0746 (in Chinese).

Jia, C.Z., Pang, X.Q., Song, Y., 2024. Basic principles of the whole petroleum system. Petrol. Explor. Dev. 51 (4), 780–794. https://doi.org/10.1016/S1876-3804(24)60506-9.

Kang, Z.M., Zhang, Y., Qin, H.J., et al., 2023. An intelligent inversion method for azimuth electromagnetic logging while drilling measurements. IEEE Access 11, 79285–79294. https://doi.org/10.1109/ACCESS.2023.3298972.

Li, H., Zhu, J., Xiong, Y.C., et al., 2020. On the depth of detection of logging-while-drilling resistivity measurements for looking-around and looking-ahead applications. Interpretation 8 (3), SL151–SL158. https://doi.org/10.1190/INT-2010-0291.1.

Li, X.H., Zhang, W.X., Chen, P., et al., 2023. Accuracy analysis and real-time inversion and imaging logging while drilling azimuth electromagnetic wave resistivity measurements. Chin. J. Geophys. 66 (9), 3990–3998. https://doi.org/10.6038/cjg2023Q0412 (in Chinese).

Li, Q., Omeragic, D., Chou, L., et al., 2005. New directional electromagnetic tool for proactive geosteering and accurate formation evaluation while drilling. In: SPWLA 46th Annual Logging Symposium. SPWLA, pp. 2005–UU.

Liu, R.M., Zhang, W.X., Chen, W.X., et al., 2025. Factors and detection capability of look-ahead logging while drilling (LWD) tools. Pet. Sci. 22 (2), 850–867. https://doi.org/10.1016/j.petsci.2024.12.024.

Marquardt, D., 1963. An algorithm for least-squares estimation of nonlinear parameters. SIAM J. Appl. Math. 11, 431–441. https://doi.org/10.1137/0111030.

Nardi, G., Martakov, S., Nikitenko, M., et al., 2010. Evaluation of parameter uncertainty utilizing resolution analysis in reservoir navigation increases the degree of accuracy and confidence in well-bore placement. In: SPWLA 51st Annual Logging Symposium. SPWLA-2010-78038.

Omeragic, D., Habashy, T., Esmersoy, C., et al., 2006. Real-time interpretation of formation structure from directional EM measurements. In: SPWLA 47th Annual Logging Symposium, SPWLA-2006-SSS.

Pakrooh, P., Pezeshki, A., Scharf, L.L., et al., 2015. Analysis of Fisher information and the Cramér–Rao bound for nonlinear parameter estimation after random compression. IEEE Trans. Signal Process. 63 (23), 6423–6428. https://doi.org/10.1109/TSP.2015.2464183.

Pardo, D., Torres-Verdín, C., 2015. Fast 1D inversion of logging-while-drilling resistivity measurements for improved estimation of formation resistivity in high-angle and horizontal wells. Geophysics 80 (2), E111–E124. https://doi.org/10.1190/geo2014-0211.1.

Schervish, M.J., 1995. Theory of Statistics. Springer, New York. https://doi.org/10.1007/978-1-4612-4250-5.

Shen, Q.Y., Wu, X.Q., Chen, J.F., et al., 2018. Solving geosteering inverse problems by stochastic hybrid monte carlo method. J. Petrol. Sci. Eng. 161, 9–16. https://doi.org/10.1016/j.petrol.2017.11.031.

Sun, K., Thiel, M., Mirto, E., el, al, 2021. New generation of ultra-high definition directional propagation resistivity for real time reservoir characterization and geosteering-while-drilling. In: SPE Middle East Oil & Gas Show and Conference. https://doi.org/10.2118/204739-MS.

Sviridov, M., Kushnir, D., Mosin, A., et al., 2023. High-performance stochastic inversion for real-time processing of LWD ultra-deep azimuthal resisitivity data. In: SPWLA 64th Annual Logging Symposium, SPWLA-2023-0082 https://doi.org/10.30632/SPWLA-2023-0082.

Tian, F., Di, Q.Y., Zheng, W.H., et al., 2023. A formation intelligent evaluation solution for geosteering. Chinese J. Geophys. (in Chinese) 66 (9), 3975–3989. https://doi.org/10.6038/cjg2023Q0689.

Wang, H.N., Yu, L., Wang, H.S., et al., 2021. A hybrid algorithm for LWD azimuthal electromagnetic responses with annular grooved drill collar. Chin. J. Geophys. 64 (5), 1811–1829. https://doi.org/10.6038/cjg2021O0243 (in Chinese).

Wang, L., Fan, Y.R., 2019. Fast inversion of logging-while-drilling azimuthal resistivity measurements for geosteering and formation evaluation. J. Petrol. Sci. Eng. 176, 342–351. https://doi.org/10.1016/j.petrol.2019.01.067.

Wang, L., Fan, Y.R., Yuan, C., et al., 2018. Selection criteria and feasibility of the inversion model for azimuthal electromagnetic logging while drilling (LWD). Petrol. Explor. Dev. 45 (5), 914–922. https://doi.org/10.11698/PED.2018.05.18 (in Chinese).

Wang, L., Li, H., Fan, Y.R., 2019. Bayesian inversion of logging-while-drilling extra-deep directional resistivity measurements using parallel tempering Markov chain Monte Carlo sampling. IEEE Trans. Geosci. Rem. Sens. 57 (10), 8026–8036. https://ieeexplore.ieee.org/document/8746808.

Wang, L., Wu, K.K., Liu, Y.M., et al., 2025. Focusing mechanism and anisotropy correction of array induction logging responses for shale reservoirs in horizontal wells. Pet. Sci. 22 (12), 4992–5004. https://doi.org/10.1016/j.petsci.2025.08.009.

Wang, T., Chemali, R., Hart, E., et al., 2007. Real-time formation imaging, dip, and azimuth while drilling from compensated deep directional resistivity. In: SPWLA 48th Annual Logging Symposium, SPWLA-2007-NNN.

Wu, H.H., Golla, C., Parker, T., Clegg, N., Monteilhet, L., 2018. A new ultra-deep azimuthal electromagnetic LWD sensor for reservoir insight. In: SPWLA 59th Annual Logging Symposium, SPWLA-2018-X.

Wu, H.H., Cull, A., Pan, L., et al., 2022a. A new generation of LWD geosteering electromagnetic resistivity tool providing multi-layer bed boundary detection, anisotropy determination, and azimuthal resistivity measurements for accurate well placement and formation evaluation. In: SPWLA 63rd Annual Logging Symposium. https://doi.org/10.30632/SPWLA-2022-0049.

Wu, Z.G., Yue, X.Z., Li, G.Y., et al., 2022b. A novel and efficient dimensionality-adaptive scheme for logging-while-drilling electromagnetic measurements modeling. J. Petrol. Sci. Eng. 215, 110572. https://doi.org/10.1016/j.petrol.2022.110572.

Yan, L., Lu, H., Shen, Q.Y., 2018. Multilayer geosteering inversion using particle swarm optimization. In: SEG International Exposition and 88th annual Meeting, segam2018-2998340. https://doi.org/10.1190/segam2018-2998340.1.

Yang, K.L., Wang, L., Fang, H., et al., 2025. A new logging-while-drilling azimuthal electromagnetic measurement for highly resistive coal mines. J. Geophys. Eng. 22 (4), 1017–1025. https://doi.org/10.1093/jge/gxaf056.

Yang, Z., Yu, Q.J., Ma, Q.M., 2020. Real time inversion and field test of LWD azimuthal electromagnetic waves based on quasi-Newton method. Petroleum Drilling Techniques 48 (3), 120–126. https://doi.org/10.11911/syztjs.2020025 (in Chinese).

Yu, L., Wang, H.N., Wang, Y.Z., et al., 2024. Adaptive global optimization of real-time boundary detection from the LWD azimuthal electromagnetic measurements in layered TI formation with arbitrarily deviated borehole. IEEE Trans. Geosci. Rem. Sens. 62, 1–15. https://doi.org/10.1109/TGRS.2024.3352901.

Yue, X.Z., Liu, T.L., Li, G.Y., et al., 2022. An analytically fast forward method of LWD azimuthal electromagnetic measurement and its geo-steering application. Chin. J. Geophys. 65 (5), 1909–1920. https://doi.org/10.6038/cjg2022P0233 (in Chinese).

Zhou, J., Li, H., Rabinovich, M., et al., 2016. Interpretation of azimuthal propagation resistivity measurements: modeling, inversion, application and discussion. In: SPWLA 57th Annual Logging Symposium, SPWLA-2016-HHHH.